Fragmented graphene synthesized on a dielectric substrate for THz applications

Rehman Hamza, Golubewa Lena, Basharin Alexey, Urbanovic Andzej, Lähderanta Erkki, Soboleva Ekaterina, Matulaitiene Ieva, Jankunec Marija, Svirko Yuri, Kuzhir Polina

DOI: 10.1088/1361-6528/ac7403

Fragmented graphene synthesized on dielectric substrate for THz applications

Hamza Rehman [1], Lena Golubewa [2], Alexey Basharin [1], Andzej Urbanovic [2], Erkki Lahderanta [3], Ekaterina Soboleva [3], Ieva Matulaitiene [2], Marija Jankunec [4], Yuri Svirko [1], Polina Kuzhir [1]*

[1]Institute of Photonics, University of Eastern Finland, Yliopistokatu 7, FI-80101 Joensuu, Finland

[2]Center for Physical Sciences and Technology, Saulėtekio av. 3, LT-10257 Vilnius, Lithuania

[3]Lappeenranta-Lahti University of Technology LUT, Yliopistonkatu 34, 53850, Lappeenranta, Finland

[4] Institute of Biochemistry, Life Sciences Center, Vilnius University, Saulėtekio al. 7, LT-10257, Vilnius, Lithuania

*corresponding author: polina.kuzhir@uef.fi

KEYWORDS**:** Graphene islands; Chemical vapor deposition; Kelvin Probe Force Microscopy; Terahertz; Direct deposition; effective conductivity; chemical potential

Abstract

Fragmented multi-layered graphene films were directly synthesized via chemical vapor deposition (CVD) on dielectric substrates with pre-deposited copper catalyst. We demonstrated that the thickness of the sacrificial copper film, process temperature and growth time essentially influence the integrity, quality, and disorder of the synthesized graphene. Atomic Force and Kelvin Probe

Force Microscopy measurements revealed the presence of nano-agglomerates and charge puddles. The potential gradients measured over the sample surface confirmed that the deposited graphene film possesses a multilayered structure, which was modelled as an ensemble of randomly oriented conductive prolate ellipsoids. THz time domain spectroscopy measurements gave *ac* conductivity of graphene flakes and homogenized graphitic films of around 1200 S/cm and 1000 S/cm, respectively. Our approach offers a scalable fabrication of the graphene structures composed of graphene flakes and having effective conductivity sufficient for a wide variety of THz applications.

1. Introduction

Graphene is a two-dimensional material of atomic thickness, with sp2 hybridized carbon atoms bonded by strong covalent bonds in the hexagonal lattice[1]. Since the first single-atom-thick crystallites were exfoliated from bulk graphite[2], graphene research has accelerated exponentially. Graphene unique properties, including high electronic mobilities, mechanical strength, and optical response is related to its structure[3] and can be controlled by the number of layers and its quality. Therefore, the synthesis and the post synthesis processes play a crucial role in the characteristics of graphene film[4] and its potential applications. Graphene electromagnetic properties can be tuned via external influences by biasing, optical pumping, and mechanical stresses, changing its chemical potential, adding the tunability into the rich palette of graphene functionalities.

A lot of progress has been made towards Dirac semimetals based tunable THz elements and graphene-based devices for THz and optical frequencies[5,6,7,8,9,10,11,12]. In contrast to graphene-based optoelectronics, graphene THz photonics not necessarily requires ideal graphene samples. For example, perfect THz shield can be composed of graphene with up to 20% of defected area including holes and grain boundaries[13], while all-graphene broadband absorbing metasurface may comprise up to 40% of highly defected meta-atoms to properly work[14].

Relatively moderate requirements for graphene quality in THz applications stimulate usage of conventional chemical vapor deposition (CVD)[15] technique for its fabrication, as the most efficient and scalable method for graphene synthesis. Large area graphene of controllable thickness has been achieved via CVD with a catalyst metal substrate. Mostly Cu or Ni foils are employed as the platform to initiate graphene synthesis using precursor carbon source gas (e.g., methane)[16].

However, efficient and scalable integration of graphene with on-demand substrates is still a challenge[17]. This is because the post-growth transfer processes result in residues and deterioration in the structure of graphene film, altering its performance significantly for the devices[18]. Although there exist advanced transfer techniques that do not affect graphene quality[19], the transfer process in principle is still time consuming and not streamlined for mass production purposes.

Alternatively, graphene can be directly deposited on the on-demand substrate without the pre-requisite post-CVD transfer processes. The idea of the sacrificial metal layer etching to collapse graphene on the dielectric has been proposed in Refs. [20, 21]. The process relies on the C atoms diffusion through the Cu grain boundaries and segregating onto the Cu-dielectric interface. Recently, CVD multilayered graphene (MLG) was obtained on Ni-Cu alloys of different compositions[15].

In our work, we evaluate the dependence of the THz response of the graphene directly synthesized on dielectric substrate on the CVD parameters and properties of the sacrificial copper film. The low - compared to Ni - carbon solubility in Cu enables more precise control of a number of graphene layers[16]. We show that THz conductivity of the graphitic films directly synthesized on a dielectric substrate is high enough to make the developed scalable synthesis technique attractive for graphene integration into various THz components[6,5].

2. Materials and methods

2.1 Graphene fabrication

2.1.1 Substrate preparation

We have considered fused silica substrate instead of e.g. germanium one because it's melting temperature is much higher, 1715°C vs 938.2°C (which is already too close to the process temperature, 900 °C). For higher quality graphene formation it is necessary to work at temperatures in the range of 900 °C or even above, so that the Cu layer can melt into liquid and allow for the diffusion of carbon atoms through copper grain boundaries towards the Cu/substrate interface [22,23].

The 0.5 mm thick fused silica (SiO_2) wafers were first treated with acetone and isopropanol for 5 minutes each using sonicator and dried at the nitrogen flow. Additionally, they were cleaned with oxygen plasma for 2 mins at flow rate of 20 sccm and radio frequency power of 150W. Afterwards, Cu film (200 nm and 500 nm) was deposited on these wafers in UNIVEX 300 thermal evaporator.

The morphological and physical properties of the nanometrically thin copper film strongly influence the formation of the graphitic structure. In the CVD process, the liquification of the copper film at the upper and lower surfaces of thin film starts at both interfaces[24] as soon as the temperature reaches the surface melting temperature, i.e. considerably lower than that of bulk copper of 1085°C. The formation of micrometer-sized droplets results in the variations of the surface energy that governs the graphene growth. The thicker the copper film, the more pronounced variations of the surface energy over the film area and more uneven growth of graphene.

2.1.2 CVD synthesis

Graphene films were fabricated in Carbolite low pressure thermal CVD. The prepared substrates were placed in quartz tube furnace and pumped down to vacuum of 0.1 mbar. To ensure clean process, the CVD chamber was cleaned with the hydrogen (20 sccm flow rate) for at least 2 hours

at room temperature. Afterwards, the furnace was heated to 900°C. At the initial temperature growth rate of 20°C/min the copper film at the dielectric surface reached the temperature of 700 °C in 35 min. At this temperature the droplets of liquified copper are formed at the air-copper interface due to the surface melting. The further increase of the temperature from 700°C to 900°C results in the propagating of the meting front into the inner area of the copper film. In order to prevent the braking of the continuous liquified copper film into droplets it was necessary to decrease the heating rate down to 10°C/min at this stage.

Once the growth temperature 900°C was reached, the samples were annealed for 30 minutes in presence of hydrogen only and in the next 30 minutes methane was also introduced into the chamber at flow rate of 40 sccm. At the end of the growth time methane flow was stopped, leaving static hydrogen, and the furnace was cooled at 10°C/min till 700°C. Then onwards, the furnace was left to cool overnight. After the CVD process, we obtained Top-graphene/Cu/Bottom-graphene/SiO_2 structure.

2.1.3 Catalyst removal

The step-by-step process to etch the interfacial copper layer and obtaining the graphene on dielectric is highlighted in supplementary materials (see Fig. S3). In our process, we are interested in the graphene layer formed at the Cu-dielectric interface. However, graphene is also formed on the top of the Cu film[23]. The top-graphene was completely removed via oxygen plasma etching at 2min/20sccm/150W.

Further Cu/Bottom-graphene/SiO_2 structure were spin coated with two different types of polymers on each type of the as-CVD grown samples to prevent the graphene on copper-dielectric substrate from harsh wet etching process: We used Polymer A (ARP-6200.18) and Polymer B (ARP-672.11, 2:3), see supplementary material for the details of the polymers and the etching process. The interfacial Cu layer in polymer/Cu/Bottom-graphene/SiO_2 was etched via RCA protocol due to penetration of the etchant through the polymer[15]. From this point onwards we will

recognize the samples as Gr200-PA, Gr200-PB (Graphitic film synthesized via 200 nm Cu film and spin coated with polymer A and B, respectively) and Gr500-PA, Gr500-PB (Graphitic film synthesized via 500 nm Cu film and spin coated with polymer A and B, respectively).

For Gr200-PA, Gr500-PA and Gr500-PB we observed successful adhesion of the polymer even after the Cu etching process, while for Gr200-PB the test gave the negative result (see Fig. S4). This indicates that type of properties of the spin-coated polymer essentially influence the graphene adhesion to the dielectric substrate. Finally, the polymer was removed from the graphene/SiO_2 by leaving in acetone bath for 24 hours, followed by Isopropyl Alcohol cleaning and nitrogen drying.

2.2 Graphitic nanostructures characterization methods

To determine the shape and morphology of the synthesized graphene/SiO_2, LEO 1500 scanning electron microscopy was used. The structural details of the fabricated samples were studied by Raman spectrometer inVia (Renishaw, UK). The laser excitation wavelength was 532 nm with incident power 50% of the total laser power (approx. 43 mW), to get a better signal to noise ratio (SNR).

The topographical features of substrates covered by graphitic films were visualized using Atomic Force microscope (AFM) (Dimension Icon, Bruker) with the controller Nanoscope 6 in tapping mode in air. The samples were studied by silicon FESP probe (nominal: resonant frequency ~75 kHz, spring constant 2.8 N/m and tip radius of 8 nm). Typical image acquisition parameters, the scan size was 2 μm and 10 μm. Resolution was 512 × 512 pixels and scan rate was 0.30 Hz.

For the surface potential measurements, we used another AFM (Multimode 8., Bruker USA) in the Kelvin Probe Force Microscopy (KPFM) mode, which utilizes a dual-pass technique. The first pass measurements are performed in the semi-contact region to map the topographical features. In the second pass the probe-sample interaction is measured in the non-contact regime by keeping the sample surface-probe distance (or lift) the same. The samples were studied by SCM-PIT-V2

Platinum Iridium coated conductive probe having resonant frequency ~75 kHz, spring constant 3 N/m and tip radius of curvature less than 25 nm. This probe is made up of highly n-doped single crystal silicon with low electrical resistivity (0.01-0.025 Ohm.cm). The scan size was 2 μm and 10 μm. Resolution was 256 × 256 pixels and scan rate was 0.20 Hz.

The Terahertz response of the graphitic films was characterized by using THz time-domain spectrometer(T-spec, EKSPLA) in transmission mode. A femtosecond laser of 800 nm wavelength and a pulse duration of 150 fs was used to generate the THz beam. The emitter and the detector were both GaAs photodetectors with Si mirror to focusing/collimating the scattered THz beam. The time-domain recorded signal was converted to frequency domain by performing Fast Fourier transform in MATLAB. Resulting amplitude and phase spectrum were obtained from the complex transfer function of the sample and a reference.

3. Experimental

3.1 SEM and Raman Spectroscopy

From the SEM images (see Fig. 1), it can be observed that obtained CVD films comprise three-dimensional graphene islands. Their distribution is homogenous, and the shapes are irregular.

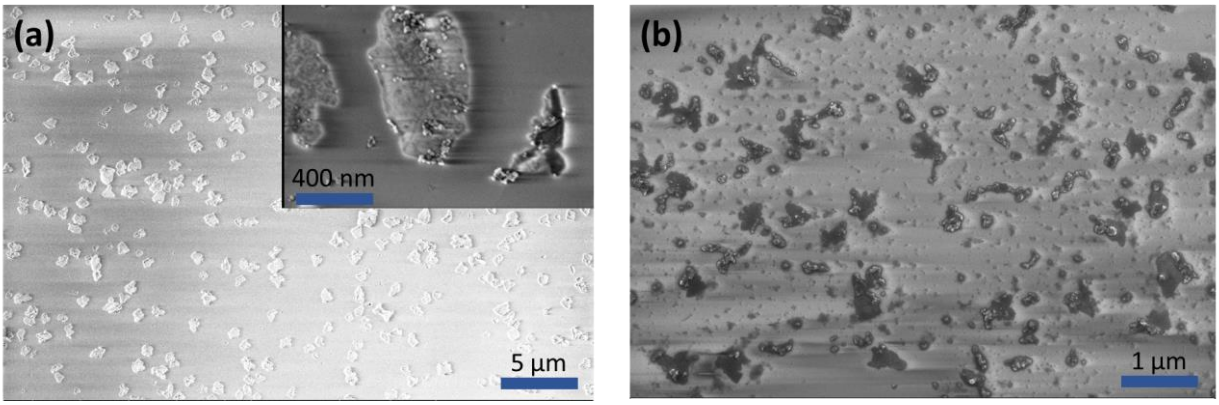

Figure 1: Top-view SEM image of (a) Gr200-PA and (b) Gr500-PA showing the graphitic film obtained on the dielectric after the top copper layer removal. The inset of (a) shows the shape of graphene island with presence of crystallinity.

The typical Raman spectra of fabricated samples can be seen in Fig. 2. Spot measurements were taken from 3 different points of each sample to check the homogeneity of the synthesized graphitic films. For all the samples, except the Gr200-PB (see Fig. S5), we were able to detect the characteristic peaks of typical graphitic nanostructure. The G-band can be seen at 1583-1586 cm^{-1} and is a direct sign of the graphitization process and its intensity can be used to determine the number of layers of graphene[1]. The G' band at 2689-2693 cm^{-1} is the signature of graphene formation[1]. The D band observed in vicinity of 1350 cm^{-1} for all the samples indicates the presence of structural defects. From the inset in Fig.2b, we detected the presence of D' band in the range 1621.0-1625.5 cm^{-1}. The, D' band belongs to the in-plane longitudinal optical phonon and the wavevector associated with this phonon is shorter. Therefore, D' band is easily activated by long-range defects such as randomly distributed charged impurities or surface charges in graphene[25].

The coverage of the graphitic film is not homogeneous in terms of thickness and quality. This is evident from the Raman mapping at G' band frequency of ~2690 cm^{-1} shown in Fig.2a. The ratio $I_G/I_{G'}$ along with full width half maximum (FWHM) and position of G' band provides an indication of the number of layers. Lorentzian peak fitting was done using OriginPro software to determine the FWHM of G and G' peaks. For the Gr200-PA, the FWHM(G') is in range 29-33 cm^{-1} and $I_G/I_{G'}$ is in range 0.63-0.83, whereas that for Gr500-PA&PB is: FWHM(G') is 38-50 cm^{-1} and $I_G/I_{G'}$ is 0.99-1.00 (see Fig. S6).

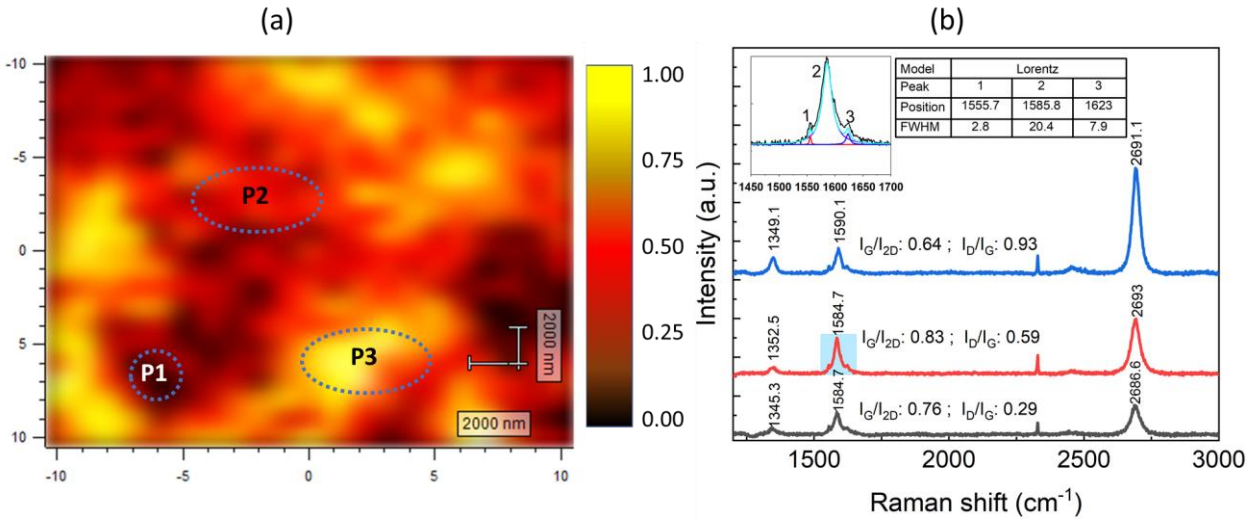

Figure 2: Raman spectroscopy measurement results for sample Gr200-PA: (a) Raman mapping at G' band (~2690 cm^{-1}). Mapping size: 10 × 10 μm with a step size 1 μm. The color bar represents the intensity normalized to baseline. (b) Spot measurements at three different points P1(black), P2(red), P3(blue). The inset plot represents the Lorentzian fit of the G-peak at the blue highlighted box. The results of the fit are presented in the inset table.

Graphene synthesized on bulk Cu foil at the same conditions (see Supplementary materials, Fig. S7) as the one grown on SiO_2 via sacrificial Cu layer is almost monolayer with $I_G/I_{G'}$= 0.178. The G' band FWHM of the graphene via Cu foil is 66 cm^{-1} which is twice that obtained for graphene via Cu film. The increase in FWHM of G' band is attributed to the defect-induced broadening. It is supported also by the intense D peak. The origin of these defects is the overlapping of graphene domains.

To conclude, having the same synthesis conditions but using bulk Cu foil we come up with worse quality of graphene compared to direct graphene growth on dielectric substrate, not requiring further time-consuming transfer.

The size of the sp^2 domains (graphene islands seen in SEM images, Fig. 1) L_{sp2} and the average distance between islands L_D can be obtained from the following equations: [26]

$$L_{sp2} = \frac{560}{E_L^4}\frac{I_G}{I_D}, \qquad L_{D(nm^2)}{}^2 = 2.4 \times 10^{-9}\lambda_L^4 \frac{I_G}{I_D},$$

where E_L and λ_L are the energy in electron volts (eV) and wavelength in nanometers, respectively for the Raman laser source. The results are presented in Table.1, where mean of 3-point measurements is taken.

We assume that the defect distance can be taken as the gap between these nano-islands and, therefore, the filling factor *p* represents the composite material comprising of graphene ellipsoids. The results of *p* calculation are mentioned in the Table 1. From this we can obtain an estimate of the concentration of graphene islands.

Table 1: Estimated parameters of the composite material comprising of graphene ellipsoids.

Sample ID	Crystallite size [nm]	Defect distance [nm]	Filling factor, p
Gr200-PA	23.17	0.155	0.9933
Gr500-PA	26.26	0.163	0.9938
Gr500-PB	21.61	0.148	0.9931

The unequal thickness at specific sites is a result of initial formation of one or more 2D monolayers followed by suppression of further layer growth being energetically unfavorable, which leads to 3D islands formation[27]. This transition from 2D to 3D island growth is associated to the elastic strain energy, which increases linearly with the film thickness. The variation of around 5.40 cm^{-1} of G band has been noticed in Gr200-PA sample. The change in G band frequency gives information of the C-C bonds and the shift in its position further allows one to suggest that the carbon nanostructures are of random shapes and orientations and, thus, giving rise to strain in the crystalline structure [25]. In Ref.[28], similar 'balling effect' have been observed where a Cu film of 60 nm thickness was sputtered onto the fused silica and then CVD process was performed at 900 ^{o}C.

The agglomeration of copper at specific sites results in reduction of film thickness at the remaining sites, thus reducing Cu catalytic activity for the formation of graphene layers at those regions.

The FWHM(G') for a monolayer graphene is ~24 cm^{-1} [1]. Even though our samples have single-Lorentzian fitted G' peak with FWHM(G') ~29-33 cm^{-1} for Gr200-PA, which is an established proof of single layer graphene, we cannot be certain that we have obtained monolayer graphene. Such value for FWHM is also possible with a twisted few layer or turbostratic graphene [29,30], which is a type of multilayer graphene with relative random orientations between carbon layers and at the same time it preserves the properties like that of monolayer graphene. Furthermore, the $I_G/I_{G'}$ ratio for all the samples is around 0.9 which suggests the presence of few layer graphene in either case [31]. The averaged ratio I_D/I_G obtained from three different point measurements for Gr200-PA,

Gr500-PA, and Gr500-PB are 0.64, 0.59, 0.63, respectively. These values suggest a moderately defective graphitic film. However, these values in addition to the position of G band in the range ~1583-1595 cm^{-1} suggests the synthesized films are well within the graphitic regime [29] . Moreover, the variation of G' band position within the same sample is ~6.4 cm^{-1}, ~3.6 cm^{-1} and ~3.84 cm^{-1} for Gr200-PA, Gr500-PA and Gr500-PB, correspondingly. This shift is significant and cannot be due to systematic variations. The origin of these shifts could be, firstly, due to the variation in thickness across the graphitic film and, secondly, due to the random doping. The bands at ~2328 cm^{-1} and ~1555 cm^{-1} are visible in all the samples and peaks are attributed to nitrogen and oxygen, respectively [32]. Since our fabrication steps involve the treatment with oxygen plasma after CVD process and the drying of the sample in a nitrogen flow, it is very much likely that, rather than environmental perturbations, this could be the reason we have some of these molecules present on graphitic film.

3.2 Atomic Force Microscopy

AFM height and phase profile images for Gr500-PA are presented in Fig. 3 whereas, for Gr200-PA and Gr500-PB see Fig. S9(a,b) in supplementary data. The results reveal the presence of nano-agglomerates with homogenous coverage. The height profile plot in Fig. 3d shows that there is a variation in the thickness in the range of few nanometers (red dashed line), with certain agglomerate structures having heights in the range of several tens of nanometers (blue dashed line).

Graphene synthesized on both 200 nm and 500 nm Cu each with different polymers have these structures. However, the density of these agglomerates is much less in the case of 200 nm Cu catalytic film was used.

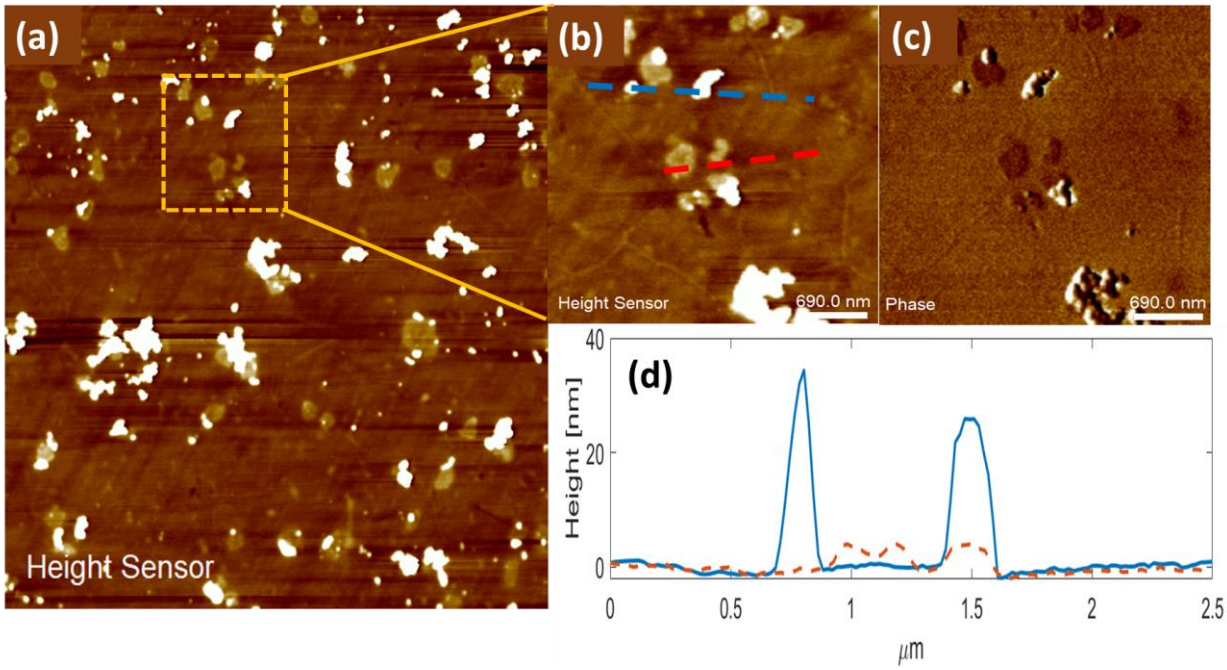

Figure 3: AFM images of the topography of Gr500-PA. (a) represents the Height profile, (b) represents height profile of the enlarged area marked with yellow dashed box in (a), (c) represents Phase profile of the same enlarged area marked with the yellow dashed box in (a), (d) represents the cross-section in the height profile (b) marked with the blue/red dashed lines in (b). The blue line represents features of greater height particle i.e approximately 30-40 nm where the red line features are very shallow particles.

From the phase map in Fig. 3c, these nano-agglomerates are out of phase with the relatively smaller features. In Ref.[23], similar nano-agglomerates have been identified as copper oxide particles and its formation has been attributed to relatively weak interaction between the copper oxide and graphitic film. The reason for the formation of these copper oxides are well explained in Ref. [33] where it is experimentally tested and concluded that possibly during the cooling process at the end of CVD process, hydrogen acts as a reducing agent and therefore, support in the formation of polygon holes exposing the underlying Cu. This Cu reacts with air and results in formation of copper oxide with sizes approximately 1 μm. Moreover, during the etching of Cu in the RCA solution bath, bubbles can be seen on the surface of the samples (see Fig. S3), the bubbles

are the sign that hydrogen peroxide of RCA solution is being decomposed by the copper oxide present.

The exact thickness of these graphitic nanostructures is still not clear due to the resolution limitations of the AFM device itself. However, the surface potential results give us sufficient evidence of the relative thicknesses within the synthesized graphene structure. In Fig. 3d the section profile across thicker part of the graphitic film shows thickness of approximately 10 nm. In table 2 the surface features of the nanostructure films are characterized by R_a (average absolute values of surface height), R_q (standard deviation of Z axis values) and Roughness R_{max} (maximum distance between highest and lowest points on surface). The results suggest that the film roughness and the estimated thickness variations in the graphitic film increases with Cu film thickness. Also, the density of these agglomerates is higher for thicker Cu film.

Table 2: Statistical analysis of the AFM images for Gr200-PA, Gr500-PA and Gr500-PB.

	Gr200-PA	**Gr500-PA**	**Gr500-PB**
Ra, nm	0.531	0.958	0.936
Rq, nm	0.725	1.23	1.32
Roughness max, nm (Area without agglomerates)	7.39	7.15	8.53
Roughness max, nm (Area with agglomerates)	131	91.9	126
Density of agglomerates /µm^2	1.530	1.78	2.19

Figure 4b shows the surface potential map of Gr200-PA along with its phase and adhesion results, presented in Fig.4c and Fig.4d, respectively. There is a strong correlation between the phase and potential response whereas the adhesion is more homogenous throughout the scanned area. The potential difference profile in Fig. 4b, represented by the section marked as white dashed box in Fig. 4a, shows that the potential difference across the graphitic film layer is measured to be around ~64.283 ± 2.694 mV, which is in good agreement with results obtained in Ref. [34], where

the potential difference between single and bilayer graphene was measured to be around ~66 mV. In addition, the mean potential difference between dielectric and graphene is 126.5 ± 35.6 mV. Similar value in the range of hundreds of millielectronvolts potential difference has also been reported in Ref. [35].

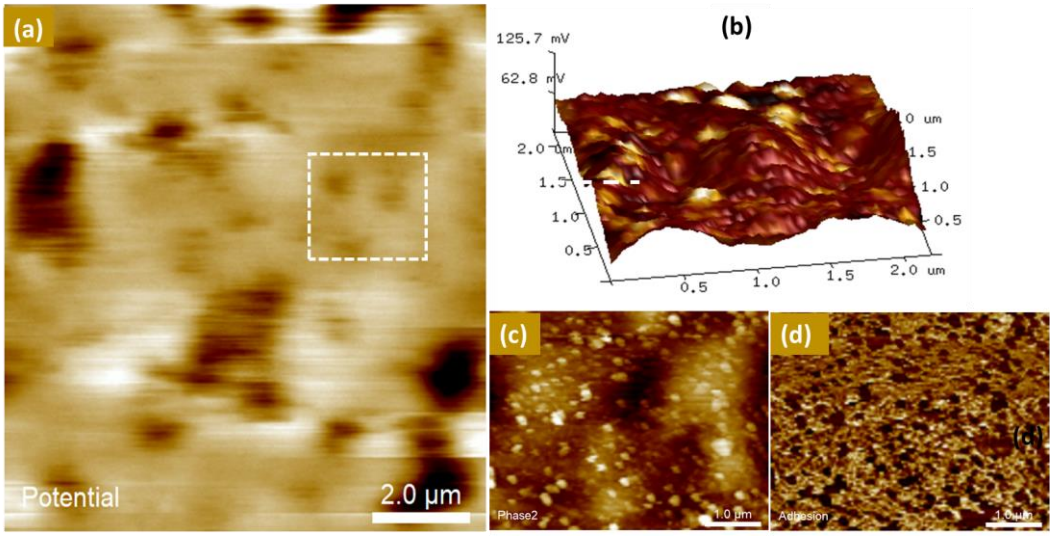

Figure 4: KPFM images for Gr200-PA a) Surface potential spatial distribution b) Enlarged image of the area marked with a white dashed box, c) Phase spatial distribution d) Adhesion map.

In Ref.[35] has been discussed that the concept of interlayer screening effect which is the underlying principle for surface potential variations as a function of graphene layer thickness. This effect is more pronounced as the number of layers in the graphene film exceeds three. This could further explain the effect of the impurities screening during the KPFM measurement. Thus, it can be inferred that the number of graphene layers is not the same from point to point, and it has some specific areas where the interlayer screen effect comes into play, as seen from the potential difference distributions.

3.3. Terahertz time-domain spectroscopy

The THz transmission (Supplementary data, Fig. S15) has been reconstructed using the equation [36]:

$$T(\omega) = \frac{E_s(\omega)}{E_{ref}(\omega)},$$

where $E_s(\omega)$ and $E_{ref}(\omega)$ are complex Fourier transforms of the measured time domain fields $E_s(t)$ and $E_{ref}(t)$, correspondingly. The value $E_s(t)$ represents the THz electric field transmitted from the graphene/dielectric substrate, whereas $E_{ref}(t)$ is the transmitted field through bare free space.

The real part of the *ac* conductivity can be obtained by the following equation applicable for thin films, i.e. $\left|\frac{n\omega d}{c}\right| \ll 1$:[37]

$$\sigma(\omega) = [\left(\frac{1}{T(\omega)}\right)(1+n_s) - (1+n_s)]/dZ_o,$$

where n_s is a substrate refractive index with value 1.8628 in THz frequencies, Z_o is free space impedance of 377Ω, d is the thickness of the film taken to be 10 nm and $T(\omega)$ is frequency dependent relative transmittance of the sample. The extracted effective conductivity, for each of the samples can be seen in Table 3.

Table 3 Extracted ac conductivity of graphitic films on fused silica substrate in THz frequency.

Sample ID	Conductivity [S/cm]		
	0.2 THz	0.6 THz	1.0 THz
Gr200-PA	1059	1081	1103
Gr500-PA	1084	1107	1129
Gr500-PB	1027	1049	1071

The conductivity of graphene is usually reported also with reference to the minimum value of graphene conductivity given by $\sigma_{min} = \pi e^2/2h$ [38]. We have obtained conductivity values of approximately 10 times bigger than that of minimum graphene conductivity. These values are smaller compared to those obtained for CVD graphene synthesized on Cu foil and transferred on to fused silica substrate, i.e. 20-90 times the value of minimum graphene conductivity [38,39].

4. Theoretical and simulation results

Basing on SEM image analysis results we model the synthesized graphitic film as an ensemble of randomly oriented conductive prolate ellipsoids with semiaxes a>b and not touching one another.

In order to reveal conductivity of the ellipsoidal graphene flakes from the experimentally measured conductivity of the composite we use the following equation:

$$\frac{p}{3}\left(\frac{\sigma_{gr}-\sigma_e}{\sigma_e+g_{\parallel}(\sigma_{gr}-\sigma_e)}+2\frac{\sigma_{gr}-\sigma_e}{\sigma_e+g_{\perp}(\sigma_{gr}-\sigma_e)}\right)+(1-p)3\frac{(\sigma_d-\sigma_e)}{2(\sigma_d+\sigma_e)}=0\ ,$$

where the polarization factors $g_{\perp}\cong\frac{1}{2}$ for prolate spheroids and $g_{\parallel}=\frac{b^2}{a^2}\ln(a/b)$, p is a concentration of graphene particles, σ_{gr} is a graphene conductivity of flakes, σ_d is a conductivity of matrix (in our case $\sigma_d=0$), and σ_e is an effective conductivity of samples, taken from the measurement data (Table 3). The frequency dependence of the graphene conductivity can be estimated using Kubo formula that accounts for the intraband and interband contributions [40,41]:

$$\sigma_S=\sigma_S^{intra}+\sigma_S^{inter},\mathrm{k}$$

$$\sigma_S^{intra}=\frac{2k_BTe^2}{\pi\hbar^2}\ln\left(2cosh\frac{E_F}{2k_BT}\right)\frac{i}{\omega+i\tau^{-1}},$$

$$\sigma_S^{inter}=\frac{e^2}{4\hbar}\left[H\left(\frac{\omega}{2}\right)+i\frac{4\omega}{\pi}\int_0^{\infty}\frac{H(\Omega)-H\left(\frac{\omega}{2}\right)}{\omega^2-4\Omega^2}d\Omega\right],$$

where T is the temperature, E_F is electrochemical potential (Fermi energy), ω *is* frequency of the electromagnetic wave and $\tau=10^{-13}$ s is the relaxation time, $H(\Omega)=\sinh\left(\frac{\hbar\Omega}{k_BT}\right)/[\cosh\left(\frac{\hbar\Omega}{k_BT}\right)+\cosh\left(\frac{E_F}{k_BT}\right)$.

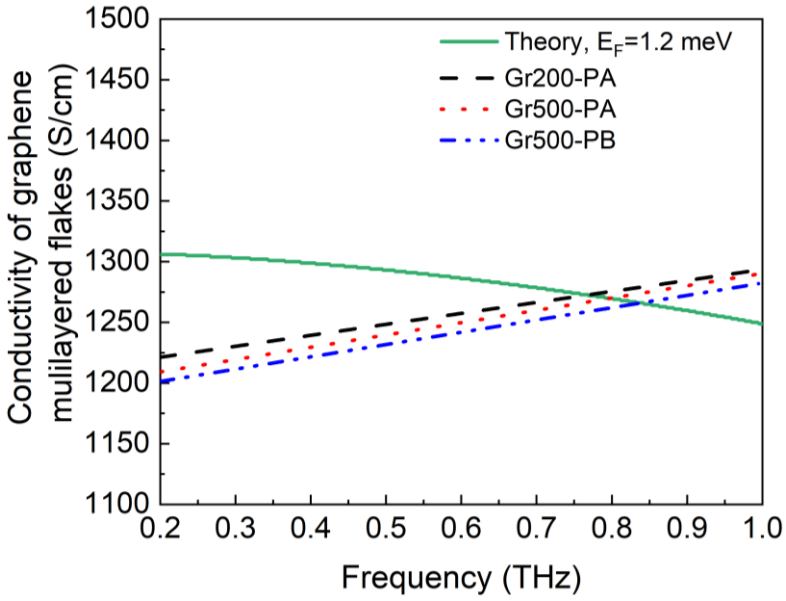

Figure 5: Calculated conductivity of the graphene flakes and theoretical conductivity obtained by Kubo formulas at chemical potential 1.2 meV.

Figure 5 shows the frequency dependence of the conductivity of graphene flakes in three samples mentioned in Table 3. At frequency of 0.6 THz, the calculated conductivity of graphene flakes for Gr200-PA, Gr500-PA and Gr500-PB are 1244 S/cm, 1258 S/cm, and 1252 S/cm, respectively. The conductivity we obtained is close to that of reported in Ref. [37] where reduced graphene oxide flakes with low electrical interconnectivity between the flakes is translated by the low conductivity values of around 900 S/cm. Second important point is the close similarity of the conductivity values obtained from the thin film equation (summed up in Table 3) and that with the proposed model above. These values of conductivity are even higher than that obtained for experimental results for CVD multilayer graphene transferred to quartz substrate [38], and so it can be further emphasized that such fragmented graphitic flakes with a filling factor resulting from direct synthesis on a dielectric substrate have enhanced conductivity in the Terahertz frequencies.

5. Discussion and conclusions

In our experiments, we developed synthesis of graphitic films directly on a dielectric substrate and demonstrated that the process parameters including thickness of the sacrificial copper film play a significant role on the integrity and quality of the obtained graphene. We found in particular that

at the temperature of around 900 °C the synthesis process demonstrated the highest repeatability in terms of the properties of the obtained graphene. The growth time is seen to have not much effect on the thickness of the MLG whatsoever, however it does have effect on the quality or the number of disorders in the graphene crystallite (see Fig. S8). Therefore, it is important to stress that the disorder in graphene can be controlled by varying the thickness of Cu film and the carbon deposition time.

The same synthesis conditions applied to the bulk Cu foil allows to synthesized more disordered mono-layered graphene in comparison with that obtained at direct growth on dielectric substrate via sacrificial Cu layer, not requiring further time consuming transfer.

The easy, transfer-free deposition of graphene on the dielectric opens further possibility of integration of these nanostructures with devices where metal contamination-free films are needed, for example biological experiments. The electrical and optical response of these graphitic films are strongly influenced by the quality of the fabricated structures. In recent studies, very few information on the electrical and topological information of the described above graphitic films has been provided. In the present study we have presented a deeper insight into these characteristics.

Our results suggest the presence of unintentional doping which could arise from the charge puddles due to structural imperfections or as a result of trapped water and/or oxygen molecules in between substrate and graphene or even Cu residue particles [42]. This is evident from the AFM and KPFM measurements (see Fig. 3 & 4). In addition, the imperfections in the graphene structure also affect the conductivity and this can be seen from the AFM statistical analysis results (Table 2), where the Gr200-PA has lower R_q and R_a values as compared to that of Gr500-PA. Moreover, the conductivity of graphene flakes comprising the CVD graphitic material directly synthesized on the dielectric substrate is as high as 1200 S/cm in THz frequency range.

Achieved parameters are competitive with other methods for the fabrication of graphene samples, for example, the spraying method demonstrating effective conductivity about 900 S/cm for reduced graphene oxide samples after a high temperature reduction process at 1000 °C [37]. Moreover, the 5 nm thick rGO film transmits less than 80%, whereas transmittance of the fabricated samples by our method has close to 97% (Supplementary data, Fig. S14).

To summarize, our approach is important for the fabrication of non-ideal graphene samples for a wide variety of applications, such as filters, waveguides, and metamaterials[3,43,44,45,46], working in THz frequency range where the fragmented samples of graphene, characterized by effective conductivity, could be useful due to electromagnetic coupling of those graphene flakes. Such a combination of a simplicity of the synthesis, high *ac* conductivity at THz frequencies and transparency in visible range makes proposed fabrication technique attractive for THz photonics applications.

Acknowledgements: This work is supported by the Academy of Finland via Flagship Programme Photonics Research and Innovation (PREIN), decision 320166, and grant 343393, and Horizon 2020 RISE DiSeTCom Project 823728. We would also like to thank Saastamoinen Foundation for providing the travel grant for the research period at FTMC, Lithuania. We acknowledge the contribution by PhD. Marian Baah for providing support in the sample preparations. Alesia Paddubskaya and Nadzeya Valynets have provided valuable insight into the THz-TDS data analysis.

REFERENCES

(1) Malard, L. M.; Pimenta, M. A.; Dresselhaus, G.; Dresselhaus, M. S. Raman Spectroscopy in Graphene. *Phys. Rep.* **2009**, *473* (5–6), 51–87. https://doi.org/10.1016/j.physrep.2009.02.003.

(2) Novoselov, K. S.; Geim, A. K.; Morozov, S. V; Jiang, D. Electric Field Effect in Atomically Thin Carbon Films. *Phys. Rev. Lett* **2004**, *306* (52), 666–669.

(3) Castro Neto, A. H.; Guinea, F.; Peres, N. M. R.; Novoselov, K. S.; Geim, A. K. The Electronic Properties of Graphene. *Rev. Mod. Phys.* **2009**, *81* (1), 109–162. https://doi.org/10.1103/RevModPhys.81.109.

(4) Wu, Y.; Wang, S.; Komvopoulos, K. A Review of Graphene Synthesis by Indirect and Direct Deposition Methods. *J. Mater. Res.* **2020**, *35* (1), 76–89. https://doi.org/10.1557/jmr.2019.377.

(5) Zhang, X.; Wang, Y.; Cui, Z.; Zhang, X.; Chen, S.; Zhang, K.; Wang, X. Carbon Nanotube-Based Flexible Metamaterials for THz Sensing. *Opt. Mater. Express* **2021**, *11* (5), 1470. https://doi.org/10.1364/ome.424693.

(6) He, X.; Lin, F.; Liu, F.; Shi, W. Tunable Terahertz Dirac-Semimetal Hybrid Plasmonic Waveguides. *Opt. Mater. Express* **2022**, *12* (1), 73. https://doi.org/10.1364/ome.445362.

(7) Leng, J.; Peng, J.; Jin, A.; Cao, D.; Liu, D.; He, X.; Lin, F.; Liu, F. Investigation of Terahertz High Q-Factor of All-Dielectric Metamaterials. *Opt. Laser Technol.* **2022**, *146* (October 2021), 107570. https://doi.org/10.1016/j.optlastec.2021.107570.

(8) He, X.; Liu, F.; Lin, F.; Shi, W. 3D Dirac Semimetal Supported Tunable TE Modes. *Ann. Phys.* **2022**, *534* (4), 1–8. https://doi.org/10.1002/andp.202100355.

(9) Ali, M. F.; Bhattacharya, R.; Varshney, G. Graphene-Based Tunable Terahertz Self-Diplexing/MIMO-STAR Antenna with Pattern Diversity. *Nano Commun. Netw.* **2021**, *30*, 100378. https://doi.org/10.1016/j.nancom.2021.100378.

(10) Varshney, G.; Giri, P. Bipolar Charge Trapping for Absorption Enhancement in a Graphene-Based Ultrathin Dual-Band Terahertz Biosensor. *Nanoscale Adv.* **2021**, *3* (20), 5813–5822. https://doi.org/10.1039/d1na00388g.

(11) Khan, M. S.; Varshney, G.; Giri, P. Altering the Multimodal Resonance in Ultrathin Silicon

Ring for Tunable THz Biosensing. *IEEE Trans. Nanobioscience* **2021**, *20* (4), 488–496. https://doi.org/10.1109/TNB.2021.3105561.

(12) Varshney, G. Reconfigurable Graphene Antenna for THz Applications: A Mode Conversion Approach. *Nanotechnology* **2020**, *31* (13). https://doi.org/10.1088/1361-6528/AB60CC.

(13) Lobet, M.; Majerus, B.; Henrard, L.; Lambin, P. Perfect Electromagnetic Absorption Using Graphene and Epsilon-near-Zero Metamaterials. *Phys. Rev. B* **2016**, *93* (23), 235424. https://doi.org/10.1103/PhysRevB.93.235424.

(14) Baah, M.; Paddubskaya, A.; Novitsky, A.; Valynets, N.; Kumar, M.; Itkonen, T.; Pekkarinen, M.; Soboleva, E.; Lahderanta, E.; Kafesaki, M.; Svirko, Y.; Kuzhir, P. All-Graphene Perfect Broadband THz Absorber. *Carbon N. Y.* **2021**, *185*, 709–716. https://doi.org/10.1016/j.carbon.2021.09.067.

(15) Dong, Y.; Guo, S.; Mao, H.; Xu, C.; Xie, Y.; Deng, J.; Wang, L.; Du, Z.; Xiong, F.; Sun, J. In Situ Growth of CVD Graphene Directly on Dielectric Surface toward Application. *ACS Appl. Electron. Mater.* **2020**, *2* (1), 238–246. https://doi.org/10.1021/acsaelm.9b00719.

(16) Li, X.; Cai, W.; An, J.; Kim, S.; Nah, J.; Yang, D.; Piner, R.; Velamakanni, A.; Jung, I.; Tutuc, E.; Banerjee, S. K.; Colombo, L.; Ruoff, R. S. Large-Area Synthesis of High-Quality and Uniform Graphene Films on Copper Foils. *Science (80-.).* **2009**, *324* (5932), 1312–1314. https://doi.org/10.1126/science.1171245.

(17) Randviir, E. P.; Brownson, D. A. C.; Banks, C. E. A Decade of Graphene Research: Production, Applications and Outlook. *Mater. Today* **2014**, *17* (9), 426–432. https://doi.org/10.1016/j.mattod.2014.06.001.

(18) Wang, D. Y.; Huang, I. S.; Ho, P. H.; Li, S. S.; Yeh, Y. C.; Wang, D. W.; Chen, W. L.; Lee,

Y. Y.; Chang, Y. M.; Chen, C. C.; Liang, C. Te; Chen, C. W. Clean-Lifting Transfer of Large-Area Residual-Free Graphene Films. *Adv. Mater.* **2013**, *25* (32), 4521–4526. https://doi.org/10.1002/adma.201301152.

(19) Zhang, G.; Gu, A. G.; Kirkman, P. M.; Lazenby, R. A.; Miller, T. S.; Unwin, P. R. Versatile Polymer-Free Graphene Transfer Method and Applications. **2016**. https://doi.org/10.1021/acsami.6b00681.

(20) Ismach, A.; Druzgalski, C.; Penwell, S.; Schwartzberg, A.; Zheng, M.; Javey, A.; Bokor, J.; Zhang, Y. Direct Chemical Vapor Deposition of Graphene on Dielectric Surfaces. *Nano Lett.* **2010**, *10* (5), 1542–1548. https://doi.org/10.1021/nl9037714.

(21) Kaplas, T.; Svirko, Y. Self-Assembled Graphene on Dielectric Micro- and Nanostructures. *Carbon N. Y.* **2014**, *70*, 273–278. https://doi.org/10.1016/j.carbon.2014.01.007.

(22) Kosterlitz, J. M.; Thouless, D. J. Long Range Order and Metastability in Two Dimensional Solids and Superfluids. (Application of Dislocation Theory). *J. Phys. C Solid State Phys.* **1972**, *5* (11), L124. https://doi.org/10.1088/0022-3719/5/11/002.

(23) Kaplas, T.; Sharma, D.; Svirko, Y. Few-Layer Graphene Synthesis on a Dielectric Substrate. *Carbon N. Y.* **2012**, *50* (4), 1503–1509. https://doi.org/10.1016/j.carbon.2011.11.020.

(24) Gromov, D. G.; Gavrilov, S. A. Manifestation of the Heterogeneous Mechanism upon Melting of Low Dimensional Systems. **2021**, *51* (10), 2135–2144. https://doi.org/10.1134/S1063783409100242.

(25) Jorio, A.; Cançado, L. G.; Malard, L. M. Vibrations in Graphene. *2D Mater. Prop. Devices* **2017**, 71–89. https://doi.org/10.1017/9781316681619.006.

(26) Sharma, R.; Chadha, N.; Saini, P. Determination of Defect Density, Crystallite Size and

Number of Graphene Layers in Graphene Analogues Using X-Ray Diffraction and Raman Spectroscopy. *Indian J. Pure Appl. Phys.* **2017**, *55* (9), 625–629.

(27) Greene, J. E. *And Microstructural Evolution : An Atomic Scale View*, Third Edit.; Elsevier Ltd., 2010. https://doi.org/10.1016/B978-0-8155-2031-3.00012-0.

(28) Dong, Y.; Xie, Y.; Xu, C.; Li, X.; Deng, J.; Fan, X.; Pan, G.; Wang, Q.; Xiong, F.; Fu, Y.; Sun, J. Transfer-Free, Lithography-Free, and Micrometer-Precision Patterning of CVD Graphene on SiO2 toward All-Carbon Electronics. *APL Mater.* **2018**, *6* (2). https://doi.org/10.1063/1.4992077.

(29) Ferrari, A. C.; Basko, D. M. Raman Spectroscopy as a Versatile Tool for Studying the Properties of Graphene. *Nat. Nanotechnol.* **2013**, *8* (4), 235–246. https://doi.org/10.1038/nnano.2013.46.

(30) Garlow, J. A.; Barrett, L. K.; Wu, L.; Kisslinger, K.; Zhu, Y.; Pulecio, J. F. Large-Area Growth of Turbostratic Graphene on Ni(111) via Physical Vapor Deposition. *Sci. Rep.* **2016**, *6* (January), 1–11. https://doi.org/10.1038/srep19804.

(31) Reina, A.; Jia, X.; Ho, J.; Nezich, D.; Son, H.; Bulovic, V.; Dresselhaus, M. S.; Kong, J. Large Area, Few-Layer Graphene Films on Arbitrary Substrates by Chemical Vapor Deposition. *Nano Lett.* **2008**, 1–6.

(32) Sandfort, V.; Goldschmidt, J.; Wöllenstein, J.; Palzer, S. Cavity-Enhanced Raman Spectroscopy for Food Chain Management. *Sensors (Switzerland)* **2018**, *18* (3). https://doi.org/10.3390/s18030709.

(33) Qi, Y.; Eskelsen, J. R.; Mazur, U.; Hipps, K. W. Fabrication of Graphene with CuO Islands by Chemical Vapor Deposition. **2012**, *28* (7), 3489–3493. https://doi.org/10.1021/la2048163.

(34) Ziegler, D.; Gava, P.; Güttinger, J.; Molitor, F.; Wirtz, L.; Lazzeri, M.; Saitta, A. M.; Stemmer, A.; Mauri, F.; Stampfer, C. Variations in the Work Function of Doped Single- and Few-Layer Graphene Assessed by Kelvin Probe Force Microscopy and Density Functional Theory. *Phys. Rev. B - Condens. Matter Mater. Phys.* **2011**, *83* (23), 1–7. https://doi.org/10.1103/PhysRevB.83.235434.

(35) Datta, S. S.; Strachan, D. R.; Mele, E. J.; Johnson, A. T. C. Surface Potentials and Layer Charge Distributions in Few-Layer Graphene Films. *Nano Lett.* **2009**, *9* (1), 7–11. https://doi.org/10.1021/nl8009044.

(36) Glover, R. E.; Tinkham, M. Conductivity of Superconducting Films for Photon Energies between 0.3 and 40kTc. *Phys. Rev.* **1957**, *108* (2), 243–256. https://doi.org/10.1103/PhysRev.108.243.

(37) Hong, J. T.; Lee, K. M.; Son, B. H.; Park, S. J.; Park, D. J.; Park, J.-Y.; Lee, S.; Ahn, Y. H. Terahertz Conductivity of Reduced Graphene Oxide Films. *Opt. Express* **2013**, *21* (6), 7633. https://doi.org/10.1364/oe.21.007633.

(38) Gabriel, D.; Sempere, B.; Colominas, C.; Ferrer-Anglada, N. THz-Conductivity of CVD Graphene on Different Substrates. *Phys. Status Solidi Basic Res.* **2015**, *252* (11), 2423–2428. https://doi.org/10.1002/pssb.201552248.

(39) Zhang, W. D.; Brown, E. R.; Pham, P. H. O.; Burke, P. AC Conductivity Parameters of Graphene Films with THz Spectroscopy. In *National Aerospace and Electronics Conference, Proceedings of the IEEE*; 2015; Vol. 2015-Febru, pp 310–312. https://doi.org/10.1109/NAECON.2014.7045824.

(40) Hanson, G. W.; Member, S. Dyadic Green ' s Functions for an Anisotropic , Non-Local Model of Biased Graphene. **2008**, *56* (3), 747–757.

(41) Llatser, I.; Kremers, C.; Cabellos-aparicio, A. Graphene-Based Nano-Patch Antenna for Terahertz Radiation. **2012**, *10*, 353–358. https://doi.org/10.1016/j.photonics.2012.05.011.

(42) Pirkle, A.; Chan, J.; Venugopal, A.; Hinojos, D.; Magnuson, C. W.; McDonnell, S.; Colombo, L.; Vogel, E. M.; Ruoff, R. S.; Wallace, R. M. The Effect of Chemical Residues on the Physical and Electrical Properties of Chemical Vapor Deposited Graphene Transferred to SiO2. *Appl. Phys. Lett.* **2011**, *99* (12), 2009–2012. https://doi.org/10.1063/1.3643444.

(43) Xia, F.; Mueller, T.; Lin, Y. ming; Avouris, P. Ultrafast Graphene Photodetector. *Opt. InfoBase Conf. Pap.* **2010**. https://doi.org/10.1364/cleo.2010.cmv1.

(44) Bonaccorso, F.; Sun, Z.; Hasan, T.; Ferrari, A. C. Graphene Photonics and Optoelectronics. *Nat. Photonics* **2010**, *4* (9), 611–622. https://doi.org/10.1038/nphoton.2010.186.

(45) Mueller, T.; Xia, F.; Avouris, P. Graphene Photodetectors for High-Speed Optical Communications. *Nat. Photonics* **2010**, *4* (5), 297–301. https://doi.org/10.1038/nphoton.2010.40.

(46) Liu, M.; Yin, X.; Ulin-Avila, E.; Geng, B.; Zentgraf, T.; Ju, L.; Wang, F.; Zhang, X. A Graphene-Based Broadband Optical Modulator. *Nature* **2011**, *474* (7349), 64–67. https://doi.org/10.1038/NATURE10067.